Rapid Communications

Ultrafast light-induced shear strain probed by time-resolved x-ray diffraction: Multiferroic $BiFeO_3$ as a case study

V. Juvé,[1] R. Gu,[1] S. Gable,[2] T. Maroutian,[2] G. Vaudel,[1] S. Matzen,[2] N. Chigarev,[3] S. Raetz,[3] V. E. Gusev,[3] M. Viret,[4] A. Jarnac,[5] C. Laulhé,[5] A. A. Maznev,[6] B. Dkhil,[7] and P. Ruello[1,*]

[1]*Institut des Molécules et Matériaux du Mans, UMR 6283 CNRS, Le Mans Université, 72085 Le Mans, France*
[2]*Centre de Nanosciences et de Nanotechnologies, UMR 9001 CNRS, Université Paris-Saclay, Palaiseau, France*
[3]*Laboratoire d'Acoustique de l'Université du Mans, UMR CNRS 6613, Le Mans Université, 72085 Le Mans, France*
[4]*SPEC UMR CEA/CNRS, Université Paris-Saclay, L'Orme les Merisiers, 91191 Cedex, Gif-sur-Yvette, France*
[5]*Université Paris-Saclay, Synchrotron Soleil, 91190 Saint-Aubin, France*
[6]*Department of Chemistry, Massachusetts Institute of Technology, Cambridge, Massachusetts 02139, USA*
[7]*Laboratoire Structures, Propriétés et Modélisation des Solides, CentraleSupélec, UMR CNRS 8580, Université Paris-Saclay, 91190 Gif-sur-Yvette, France*

(Received 21 July 2020; accepted 1 December 2020; published 17 December 2020)

Enabling the light control of complex systems on ultrashort timescales gives rise to rich physics with promising applications. Although crucial, the quantitative determination of both the longitudinal and the shear photoinduced strains still remains challenging. Here, by scrutinizing asymmetric Bragg peaks pairs ($\pm h01$) in $BiFeO_3$ using picosecond time-resolved x-ray diffraction experiments, we simultaneously determine the longitudinal and shear strains. Importantly, we reveal a difference in the dynamical response of the longitudinal strain with respect to the shear one due to an interplay of quasilongitudinal and quasitransverse acoustic modes, well reproduced by our model. Finally, we show that the relative amplitude of those strains can be explained only if both thermal and nonthermal processes contribute to the acoustic phonon photogeneration process.

DOI: 10.1103/PhysRevB.102.220303

Longitudinal strain in matter is represented by a compressional field with a diagonal tensor in the principal coordinate system. On the contrary, the shear strain tensor has only off-diagonal terms associated with a zero volume change. Specifically, it is the *curl* part (rotational motion) of the atomic displacement which propagates at the shear velocity in matter [1], i.e., shear acoustic phonons carry angular momentum. In the context of ultrafast science in condensed matter, this specific symmetry of atomic displacements has several impacts: for instance, the light-induced picosecond shear pulse can be used to probe ultrafast friction in soft matter [2,3] or induce ultrafast rotation of light polarization [4–7]. It has been also shown that during an ultrafast light-induced demagnetization process the shear acoustic phonons can exchange angular momentum with spins through the Einstein–de Haas effect [8,9] or sometimes called the Richardson effect [10,11]. Beyond these two examples, generating shear motion with light has received a great deal of attention in general, and several demonstrations of this phenomenon have been reported in different materials including multiferroic oxides, such as $BiFeO_3$ (BFO) [12–14], piezoelectric semiconductors GaN [15], GaAs [4], metals [4,5,16,17], or spin-crossover compounds [18] for citing a few. Despite this active and continuous effort, the underlying physics of the light-induced shear strain generation remains unclear since the quantitative measurement of the shear strain amplitude is lacking. X-ray or electron-diffraction methods appear as natural experimental tools to quantify the light-induced strain. However time-resolved x-ray [9,19–29] or electron- [30–32] diffraction experiments have mostly been applied to extract the longitudinal strain. A few attempts at a quantitative evaluation of the light-induced shear strain amplitude have been recently reported in a crystalline organic thin film by time-resolved x-ray diffraction but with 100 ps of resolution only [33]. Time-resolved electron diffraction has also been used to reveal shear waves generated either by light pulses in layers of VTe_2 [32] or by acoustic mode conversion in a graphite membrane [31].

In this Rapid Communication we apply picosecond time-resolved x-ray diffraction and measure the transient evolution of the asymmetric Bragg reflection pairs ($\pm h01$) to quantitatively determine the photoinduced shear and longitudinal strains in a BFO single crystal. We evidence different temporal behaviors between the two strains indicating that the BFO unit cell starts to expand during the first tens of picoseconds after the arrival of the light pulse and only then undergoes a shear deformation. This peculiar dynamic is well reproduced by our modeling based on strain wave propagation theory. Moreover, quantitative information on the strain amplitudes sheds new light on the photoinduced generation process and indicates that both thermal and nonthermal processes are at play. Beyond the BFO case, our Rapid Communication shows that this approach is very versatile and can be employed to access the in-plane atomic displacements in any kind of structure where an in-plane symmetry breaking is present or initiated by an external stimulus including light pulses.

*pascal.ruello@univ-lemans.fr

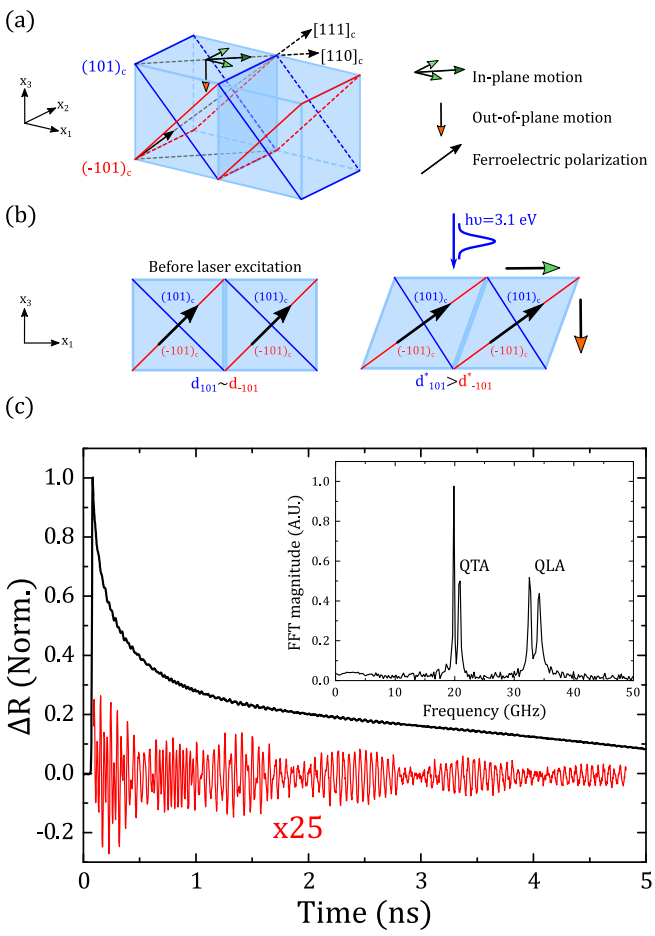

FIG. 1. (a) Three-dimensional view of the BFO pseudocubic unit cell with displacement vector associated with the longitudinal and shear photoinduced strains (orange and green arrows). The black arrow is the $BiFeO_3$ ferroelectric polarization pointing along the $[111]_c$ direction. (b) Side view of the $BiFeO_3$ pseudocubic unit cell before and after the laser excitation showing the in-plane and out-of-plane motions. (c) Transient optical reflectivity signal of the BFO single crystal measured with 400-nm pump and 800-nm probe beams. The red line shows the acoustic phonon signal once the base line has been subtracted. The inset shows the fast Fourier transform with the quasilongitudinal and quasitransverse acoustic phonon modes.

We first describe theoretically how the unit cell is distorted in the presence of longitudinal and shear strains. Knowing that the rhombohedral distortion in bulk BFO is weak (equivalent rhombohedral angle $\approx 89.5^\circ$ and pseudocubic parameter $a_0 \approx 3.96$ Å), we consider the pseudocubic representation of the BFO lattice as depicted in Fig. 1(a) (see note 1 of the Supplemental Material for the description of the different crystallographic frames [34]). At equilibrium (before laser excitation), the interplanar distances of the $(101)_c$ and $(-101)_c$ planes are nearly identical ($d_{101} \approx d_{-101}$). As the laser pulse impinges on the $(001)_c$ surface of BFO and due to the existence of in-plane symmetry breaking caused by the ferroelectric polar order, the laser-matter interaction leads to the generation of shear motion [12–14,35] in addition to the longitudinal strain. Importantly, the shear strain is expected to lead to an asymmetric change in the interplanar distances d^*_{101} and d^*_{-101} with $d^*_{101} > d^*_{-101}$ as displayed in Fig. 1(b). This principle can be applied to all $(\pm h01)$ planes. Note that the atomic displacements associated to the longitudinal and shear strain are symbolized with orange and green arrows, respectively, in Figs. 1(a) and 1(b). The relation between the interplanar distance $d^*_{\pm h01}$ and the longitudinal η_L and shear η_S strains is established in the Supplemental Material note 2 as [34]

$$d^*_{\pm h01} = d_{\pm h01}\left(1 + \frac{\eta_L \pm |h|\frac{\eta_S}{\sqrt{2}}}{1+h^2}\right). \tag{1}$$

Measuring both d^*_{h01} and d^*_{-h01} then allows disentangling the photoinduced longitudinal and shear strains. They cast as

$$\eta_L = \frac{1+h^2}{2}\left[\frac{d^*_{h01}-d_{h01}}{d_{h01}} + \frac{d^*_{-h01}-d_{-h01}}{d_{-h01}}\right],$$
$$\eta_S = \frac{1+h^2}{\sqrt{2}|h|}\left[\frac{d^*_{h01}-d_{h01}}{d_{h01}} - \frac{d^*_{-h01}-d_{-h01}}{d_{-h01}}\right]. \tag{2}$$

The experiments make use of a pump-probe scheme where a femtosecond pulse with a photon energy of 3.1 eV, thus, higher than the band-gap ($E_g \approx 2.6$ eV), generates strain pulses in a single BFO crystal oriented along the $[001]_c$ direction [36]. The propagation of the strain pulses is then followed in the crystal's depth either by another femtosecond pulse with a photon energy of 1.5 eV or by a synchronized hard x-ray picosecond pulse. In the all-optical pump-probe experiment, detection with a photon energy below the band gap allows detecting the emitted coherent acoustic phonons over a long time of propagation by means of Brillouin scattering. In Fig. 1(c), the change in the probe's reflectivity is plotted as a function of the pump-probe delay. Once the slow relaxation signal is subtracted, the coherent acoustic phonon contribution can be isolated [red curve in Fig. 1(c)], and its spectrum extracted with a fast Fourier transform [inset of Fig. 1(c)]. In the case of BFO, the existence of the symmetry plane $(110)_c$ being perpendicular to the irradiated surface restricts the light-induced atomic motions within this $(110)_c$ plane and, consequently, suppresses the pure shear motion. It turns out that only quasilongitudinal (QLA) and quasitransverse (QTA) modes are excited [12,13]. In the detection process, the QLA and QTA modes are each split into two as shown in Fig. 1(c) due to BFO's optical birefringence as already discussed in a previous report [35]. The corresponding sound velocities are $V_{QLA} = 4970 \pm 30$ m s^{-1} and $V_{QTA} = 3020 \pm 30$ m s^{-1} as deduced from the Brillouin frequency equation $f_B = 2n_{\text{probe}}V/\lambda_{\text{probe}}$ where n_{probe} is the BFO ordinary or extraordinary refractive index at the probing wavelength λ_{probe} [37].

Regarding time-resolved x-ray diffraction experiments, the measurements were performed at the SOLEIL Synchrotron on the CRISTAL beamline in the low-α mode with hard x-ray pulses of 7.155-keV energy and 12-ps duration [38]. The x-ray grazing incidence geometry [1°, see Fig. 2(a)] was used to match the optically excited and probed volumes. The effective penetration depths of the 3.1-eV pump beam and of the x-ray beam can be estimated to $\xi_p \approx 40$ nm [37] and $\xi_X \approx 70$ nm [39], respectively. In this diffraction geometry, the Bragg angle θ is deduced from the relation $\cos(2\theta) = \cos(\delta)\cos(\gamma)$. The pump beam size on the sample was about twice as large

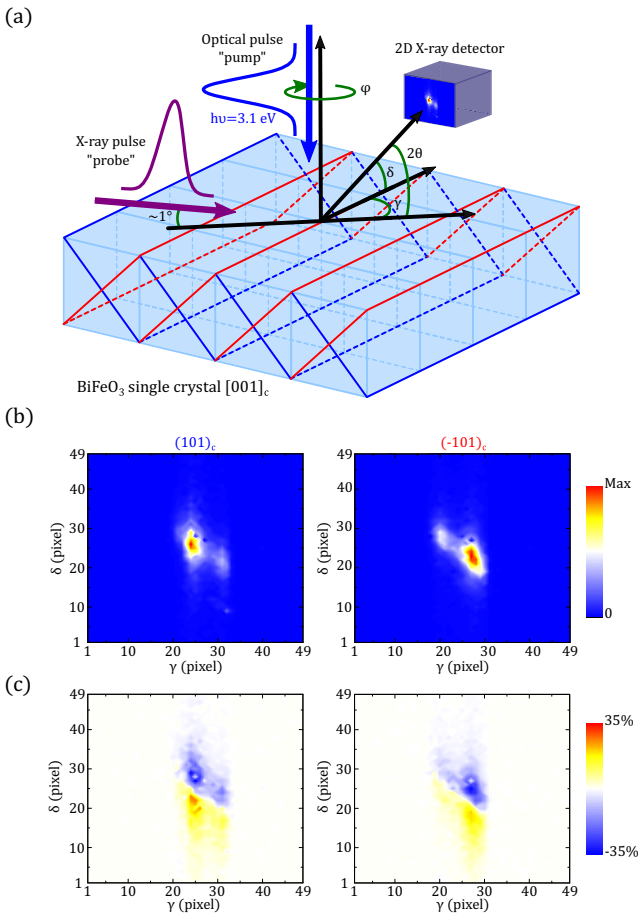

FIG. 2. (a) Scheme of the time-resolved x-ray diffraction in the grazing incidence geometry. (b) Reciprocal space imaging of the $(101)_c$ and $(-101)_c$ Bragg diffraction peaks at equilibrium. The positions (γ, δ) of the $(101)_c$ and $(-101)_c$ Bragg diffraction peaks are $(26.1874°, 26.0802°)$ and $(26.0367°, 25.6879°)$, respectively, with a camera resolution of 8.64×10^{-3} °/pixel. (c) Differential reciprocal space imaging of the $(101)_c$ and $(-101)_c$ Bragg diffraction peaks at a time delay of 200 ps and at a fluence of 3 mJ cm^{-2}.

as the x-ray probe beam size and the pump beam fluence was set to either 1.5 or 3 mJ cm^{-2}. The $(\pm h01)_c$ Bragg peaks were recorded as the function of the pump-probe delay with gateable detector XPAD3.2 [40]. The sample was rotated by 180° to switch between $(h01)_c$ and $(-h01)_c$ Bragg diffraction peaks after a complete pump-probe delay scan. Few scans were recorded for each set of experimental parameters, namely, $\pm h$ and the pump fluence. Figure 2(b) shows typical images of the $(101)_c$ and $(-101)_c$ Bragg peaks before laser excitation. Those are split, which indicates the presence of a secondary small ferroelectric-ferroelastic domain in the BFO single crystal. After laser excitation, the $(101)_c$ and $(-101)_c$ peaks evolve as depicted in Fig. 2(c) for a pump-probe delay of 200 ps. The two-dimensional center-of-mass $[\gamma(t), \delta(t)]$ was calculated for each pump-probe delay, which allowed us to extract the time dependence of the relative interplanar distance $\Delta d(t)/d$ after laser excitation (see Supplemental Material note 3 [34]).

The results for $(101)_c$, $(-101)_c$, $(201)_c$, and $(-201)_c$ lattice planes are displayed in Figs. 3(a) and 3(b) for the first 300 ps. As expected, one can clearly observe nonequivalent $\Delta d/d$ photoinduced dynamics for the $(h01)_c$ and $(-h01)_c$ lattice planes after time-delay zero. The transient longitudinal and shear strains were derived by using Eq. (2). The results are displayed in Fig. 3(c) and show a plateaulike response after roughly 100 ps for both strains with a maximum amplitude of $\eta_L^{\max} \approx 9 \times 10^{-4}$ and $\eta_S^{\max} \approx 1.5 \times 10^{-4}$ $(\eta_L^{\max}/\eta_S^{\max} \approx 6)$. Strikingly, one can clearly observe a time delay between the onsets of the longitudinal and shear strains (within the blue-shaded area) in Fig. 3(c). The maximum of the longitudinal strain is reached at around 40 ps whereas that of the shear strain is only reached after around 50–70 ps. We also note a possible negative shear strain in the first 20 ps, but it is difficult to conclude at the moment due to the error bars. Nevertheless, it is clear that the necessary time for the longitudinal and shear strains to reach the maximum positive amplitude is different: An asynchronous behavior exists and has never been observed before as previous works were restricted only to the photoinduced longitudinal strain [24,26,27]. Changing the laser pump fluence to 1.5 mJ cm^{-2} gives the same general temporal behavior but with half the amplitude, thus, confirming the linear response of the system to the laser excitation (not shown).

The experimental data were analyzed by modeling the laser-induced strain propagation in the BFO single crystal. We considered only the lattice dynamics (waves propagation) and the pump (optical) and probe (x-ray) pulses penetration depths as parameters. We recall that as the trigonal axis is not aligned with the propagation axis of the acoustic modes x_3, the generated QLA and QTA modes have components both in plane, along the $[110]_c$ direction, and out of plane, along the $[001]_c$ direction [see Fig. 3(d)]. Therefore, we can write the total shear and longitudinal strains as

$$\eta_S(t, x_3) = \eta_S^{QTA} f(t, x_3, V_{QTA}) + \eta_S^{QLA} f(t, x_3, V_{QLA}),$$
$$\eta_L(t, x_3) = \eta_L^{QTA} f(t, x_3, V_{QTA}) + \eta_L^{QLA} f(t, x_3, V_{QLA}), \quad (3)$$

where η_S^{QTA} (η_S^{QLA}) and η_L^{QTA} (η_L^{QLA}) are the in-plane and out-of-plane components of the QTA (QLA) mode propagating at the velocity V_{QTA} (V_{QLA}) and $f(t, x_3, V_{QTA,QLA})$ is the function describing the space and time dependence of the strain associated with the QTA or the QLA modes in the framework developed by Thomsen and co-workers [41] (Supplemental Material note 4 [34]). The vector components $\vec{\eta}_{QLA} = (-1, 4.8)$, $\vec{\eta}_{QTA} = (4.8, 1)$, and their associated velocities $(V_{QLA} = 4710$ and $V_{QTA} = 2480$ m s$^{-1})$ were calculated by using the rotated elastic stiffness tensor in the Christoffel framework (see Supplemental Material note 4 [34]) with the elastic constants measured and calculated from the work of Borissenko *et al.* [42] and Shang *et al.* [43], respectively (see Supplemental Material note 4 [34]). To simulate the transient lattice distortion, we assume the kinematic approximation of x-ray diffraction to be valid. In the kinematic approximation of diffraction theory, the measured strains are average strains weighted by the transmission factor of x rays along the

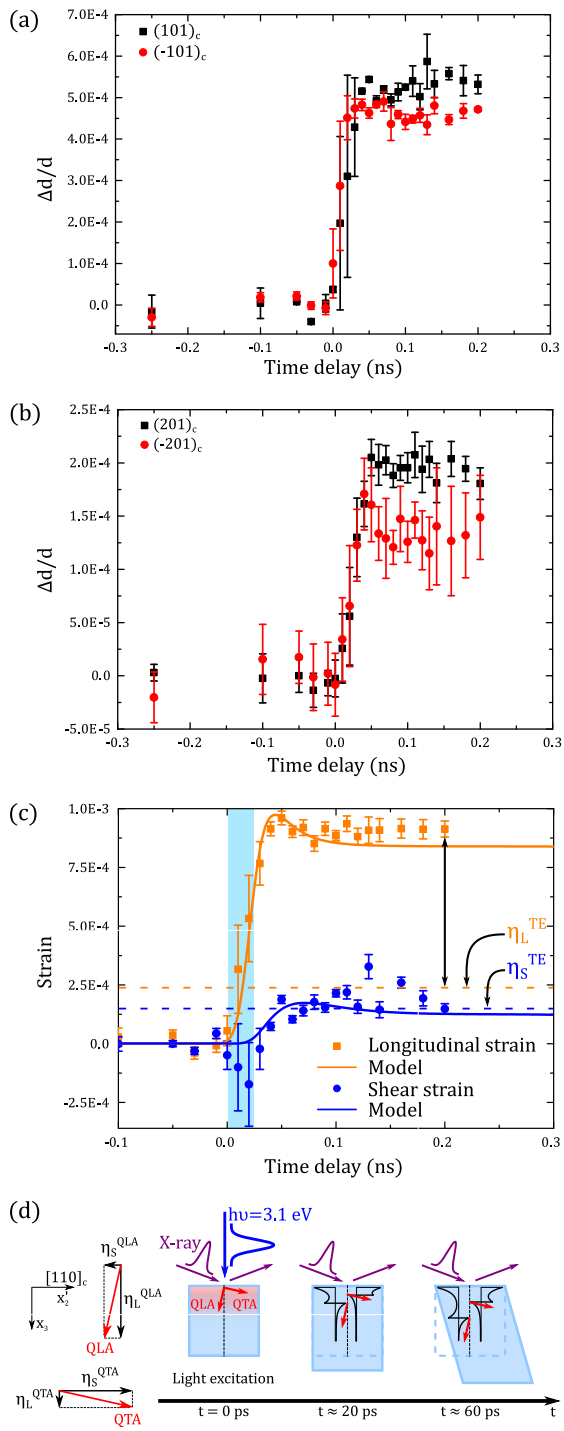

FIG. 3. (a) Time dependence of the relative variation of the interplanar distance for the $(101)_c$ and $(-101)_c$ planes. (b) Same as (a) but for the $(201)_c$ and $(-201)_c$ planes. (c) Comparison of the experimentally determined photoinduced longitudinal $\langle \eta_L \rangle(t)$ and shear strains $\langle \eta_S \rangle(t)$ calculated from Eq. (2) (symbols) with the ones (lines) deduced from Eqs. (3) and (4) based on the theory of acoustic waves propagation and x-ray scattering. The horizontal dashed lines represent the estimated maximum strain coming from the laser-induced heating effect [thermoelastic effect (TE), see the text]. (d) Sketch of the time-dependent shape of the unit cell (from a cubic to a trapezoidal form) related to the spatial separation of the in-plane and out-of-plane strain components of the QLA and QTA modes.

diffraction path,

$$\langle \eta_{L,S} \rangle(t) = \frac{\int_{x_3=0}^{\infty} dx_3 e^{-[L(x_3)]/\Lambda} \eta_{L,S}(t, x_3)}{\int_{x_3=0}^{\infty} dx_3 e^{-[L(x_3)]/\Lambda}}, \tag{4}$$

$L(x_3)$ refers to the length traveled by the x-ray beam within the BFO sample when diffracted at the depth x_3. Its expression, which depends not only on x_3, but also on the diffraction angles, is derived in the Supplemental Material note 5 [34]. The attenuation length of x rays $\Lambda = 4.22\ \mu$m accounts for absorption due to the photoelectric effect.

The curves in Fig. 3(c) correspond to the calculated strains by using Eq. (4) and are in good agreement with the experimental data (squares and circles) by adjusting $\vec{\eta}_{QLA}$ and $\vec{\eta}_{QTA}$ amplitudes in order to constrain the vectors orthogonality. Our model reproduces this asynchronous effect that originates from the opposite sign of the in-plane components of the QLA and QTA modes $[\vec{\eta}_{QLA}(x_2')$ and $\vec{\eta}_{QTA}(x_2')]$ which leads to a near cancellation of the total shear strain at early times ($\lessapprox 20$ ps). As the acoustic modes have different velocities, this effect fades away as the acoustic modes separate in space at longer times as sketched in Fig. 3(d). The rising times are also very well reproduced by our model underlining the minimal effect of the carrier or heat diffusion for such timescales. Our model does not predict at the moment a possible negative shear strain during the first 20 ps as experimentally revealed [Fig. 3(c)].

We now discuss the physics underlying the femtosecond generation of the longitudinal and the shear waves in BFO. In absorbing and piezoelectric materials, the photoinduced strains can be initiated by thermal (TE) or nonthermal [inverse piezoelectric effect (PE) and deformation potential] mechanisms [16,17,41]. For our experimental conditions, we estimate the mean temperature elevation and the mean photoexcited carriers density in the probed region to be $\langle \Delta T \rangle \approx 13$ K and $\langle N \rangle \approx 4 \times 10^{20}$ cm^{-3} for a laser fluence of 3 mJ cm^{-2} (see Supplemental Material notes 6 and 7 [34]). We neglect carriers and heat diffusion and restrict our assessments to the pump-probe volume, which is constrained by the light and x-ray penetration depths. By taking into account the anisotropic thermal expansion coefficient [44], one can extract the corresponding amplitude of the longitudinal strain $\eta_L^{\mathrm{TE}} \approx 2.4 \times 10^{-4}$ and shear strain $\eta_S^{\mathrm{TE}} \approx 1.5 \times 10^{-4}$ for the thermoelastic mechanism (see Supplemental Material note 6 [34]). Although the estimated shear strain amplitude from the TE is close to the experimental one, the estimated longitudinal one is ~4 times smaller [see the dashed lines in Fig. 3(c)]. This strongly suggests that there is a non-negligible contribution from the nonthermal processes to the total photoinduced longitudinal strain. It is difficult to estimate the deformation potential mechanism because there is a lack of documented experimental values for the electron-hole longitudinal and shear acoustic phonons deformation potential constants in the literature. Nevertheless, an isotropic electron-hole acoustic phonon deformation potential constant can be derived from high-pressure measurements [45] (see Supplemental Material note 6 [34]) and it leads to an average contraction of the BFO's lattice, similar to first-principles calculation results [46], in contradiction with our experimental observations. As for the

inverse piezoelectric effect, the transient internal depolarizing field due to the photoexcited carriers remains difficult to estimate. However, using the tabulated piezoelectric coefficients [47–49], one can estimate the ratio of the longitudinal and shear strains, which does not depend on the internal depolarizing field (see Supplemental Material note 6 [34]). It reads $\eta_L^{PE}/\eta_S^{PE} \lesssim 1$ indicating that the inverse piezoelectric effect cannot solely drive the transient strains as well as be ruled out from the total photoinduced strains.

In conclusion, we have determined quantitatively and simultaneously the photoinduced longitudinal and shear strains at the picosecond timescale in a BFO single crystal. We evidenced that the BFO's unit cell initially starts to expand during the first tens of picoseconds after the arrival of the light pulse and then later, after around 20 ps, undergoes a shear deformation. Our theoretical modeling reproduces the experimental results and brings into prominence the interplay of the propagating quasilongitudinal and the quasitransverse acoustic modes on the measured strains in the unit cell. We also underline that the experimental photoinduced strains amplitude has to be explained by a contribution of both thermal and nonthermal mechanisms. Finally, our results demonstrate the strong potential of time-resolved x-ray diffraction for extracting the temporal evolution of both in-plane and out-of-plane lattice deformations, paving the way to explore any kind of materials where in-plane symmetry breaking can be modulated by an ultrashort light pulse or any other stimulus.

We acknowledge SOLEIL for provision of synchrotron radiation at the CRISTAL beamline (Proposal No. 20181798). We thank the French National Research Agency (ANR) for support with the Project UP-DOWN (Project No. ANR-18-CE09-0026-04) and SANTA (Project No. ANR-19-CE24-0018-03). The contribution by A.A.M. was supported by the U.S. Department of Energy, Office of Basic Energy Sciences award DE-SC0019126. V.J., R.G., G.V., and P.R. acknowledge the International Laboratory IM-LED. We thank C. Paillard, L. Bellaiche, R. A. Duncan, H. D. Shinv, and M. Bargheer for fruitful discussions.

[1] B. A. Auld, *Acoustic Fields and Waves in Solids*, 2nd ed. (Krieger, Malabar, 1990), Vol. 2.

[2] T. Pezeril, C. Klieber, S. Andrieu, and K. A. Nelson, Optical Generation of Gigahertz-Frequency Shear Acoustic Waves in Liquid Glycerol, Phys. Rev. Lett. **102**, 107402 (2009).

[3] C. Klieber, T. Hecksher, T. Pezeril, D. H. Torchinsky, J. C. Dyre, and K. A. Nelson, Mechanical spectra of glass-forming liquids. II. Gigahertz-frequency longitudinal and shear acoustic dynamics in glycerol and DC704 studied by time-domain Brillouin scattering, J. Chem. Phys. **138**, 12A544 (2013).

[4] O. Matsuda, O. B. Wright, D. H. Hurley, and V. E. Gusev, Coherent Shear Phonon Generation and Detection with Ultrashort Optical Pulses and K. Shimizu, Phys. Rev. Lett. **93**, 095501 (2004).

[5] T. Pezeril, P. Ruello, S. Gougeon, N. Chigarev, D. Mounier, J.-M. Breteau, P. Picart, and V. Gusev, Generation and detection of plane coherent shear picosecond acoustic pulses by lasers: Experiment and theory, Phys. Rev. B **75**, 174307 (2007).

[6] O. Matsuda, O. B. Wright, D. H. Hurley, V. Gusev, and K. Shimizu, Coherent shear phonon generation and detection with picosecond laser acoustics, Phys. Rev. B **77**, 224110 (2008)

[7] D. Mounier, P. Picart, P. Babilotte, P. Ruello, J. M. Breteau, T. Pézeril, G. Vaudel, M. Kouyaté, and V. Gusev, Jones matrix formalism for the theory of picosecond shear acoustic pulse detection, Opt. Express **18**, 6767 (2010).

[8] Einstein and de Haas, Verh. Dtsch. Phys. Ges. **17**, 152 (1915).

[9] C. Dornes, Y. Acremann, M. Savoini, M. Kubli, M. J. Neugebauer, E. Abreu, L. Huber, G. Lantz, C. A. F. Vaz, H. Lemke, E. M. Bothschafter, M. Porer, V. Esposito, L. Rettig, M. Buzzi, A. Alberca, Y. W. Windsor, P. Beaud, U. Staub, D. Zhu, S. Song, J. M. Glownia, and S. L. Johnson, The ultrafast Einstein-de Haas effect, Nature (London) **565**, 209 (2019).

[10] O. W. Richardson, A mechanical effect accompanying magnetization, Phys. Rev. **26**, 248 (1908).

[11] M. Ganzhorn, S. Klyatskaya, M. Ruben, and W. Wernsdorfer, Quantum Einstein-de Haas effect, Nat. Commun. **7**, 11443 (2016).

[12] P. Ruello, T. Pezeril, S. Avanesyan, G. Vaudel, V. Gusev, I. C. Infante, and B. Dkhil, Photoexcitation of gigahertz longitudinal and shear acoustic waves in $BiFeO_3$ multiferroic single crystal, Appl. Phys. Lett. **100**, 212906 (2012)

[13] M. Lejman, G. Vaudel, I. C. Infante, P. Gemeiner, V. E. Gusev, B. Dkhil, and P. Ruello, Giant ultrafast photo-induced shear strain in ferroelectric $BiFeO_3$, Nat. Commun. **5**, 4301 (2014).

[14] M. Lejman, C. Paillard, V. Juvé, G. Vaudel, N. Guiblin, L. Bellaiche, M. Viret, V. Gusev, B. Dkhl, and P. Ruello, Magnetoelastic and magnetoelectric couplings across the antiferromagnetic transition in multiferroic $BiFeO_3$, Phys. Rev. B **99**, 104103 (2019).

[15] Y.-C. Wen, T.-S. Ko, T.-C. Lu, H.-C. Kuo, J.-I. Chyi, C.-K. Sun, Photogeneration of coherent shear phonons in orientated wurtzite semiconductors by piezoelectric coupling, Phys. Rev. B **80**, 195201 (2009)

[16] P. Ruello and V. E. Gusev, Physical mechanisms of coherent acoustic phonons generation by ultrafast laser action, Ultrasonics **56**, 21 (2015).

[17] V. Gusev and A. Karabutov, *Laser Optoacoustics* (AIP, New York, 1993).

[18] T. Parpiiev, M. Servol, M. Lorenc, I. Chaban, R. Lefort, E. Collet, H. Cailleau, P. Ruello, N. Daro, G. Chastanet, and T. Pezeril, Ultrafast non-thermal laser excitation of gigahertz longitudinal and shear acoustic waves in spin-crossover molecular crystals [Fe(PM-AzA)2(NCS)2], Appl. Phys. Lett. **111**, 179901 (2017)

[19] A. M. Lindenberg, I. Kang, S. L. Johnson, T. Missalla, P. A. Heimann, Z. Chang, J. Larsson, P. H. Bucksbaum, H. C. Kapteyn, H. A. Padmore, R. W. Lee, J. S. Wark, and R. W. Falcone, Time-Resolved X-Ray Diffraction from Coherent

Phonons during a Laser-Induced Phase Transition, Phys. Rev. Lett. **84**, 111 (2000).

[20] D. A. Reis, M. F. DeCamp, P. H. Bucksbaum, R. Clarke, E. Dufresne, M. Hertlein, R. Merlin, R. Falcone, H. Kapteyn, M. M. Murnane, J. Larsson, Th. Missalla, and J. S. Wark, Probing Impulsive Strain Propagation with X-Ray Pulses, Phys. Rev. Lett. **86**, 3072 (2001).

[21] S. W. Teitelbaum, T. Henighan, Y. Huang, H. Liu, M. P. Jiang, D. Zhu, M. Chollet, T. Sato, . D. Murray, S. Fahy, S. O'Mahony, T. P. Bailey, C. Uher, M. Trigo, and D. A. Reis, Direct Measurement of Anharmonic Decay Channels of a Coherent Phonon, Phys. Rev. Lett. **121**, 125901 (2018)

[22] J. Larsson, A. Allen, P. H. Bucksbaum, R. W. Falcone, A. Lindenberg, G. Naylor, T. Missalla, D. A. Reis, K. Scheidt, A. Sjögren, P. Sondhauss, M. Wulff, and J. S. Wark, Picosecond X-ray diffraction studies of laser-excited acoustic phonons in InSb, Appl. Phys. A **75**, 467 (2002).

[23] C. v. Korff Schmising, M. Bargheer, M. Kiel, N. Zhavoronkov, M. Woerner, T. Elsaesser, I. Vrejoiu, D. Hesse, and M. Alexe, Coupled Ultrafast Lattice and Polarization Dynamics in Ferroelectric Nanolayers, Phys. Rev. Lett. **98**, 257601 (2007).

[24] D. Schick, M. Herzog, H. Wen, P. Chen, C. Adamo, P. Gaal, D. G. Schlom, P. G. Evans, Y. Li, and M. Bargheer, Localized Excited Charge Carriers Generate Ultrafast Inhomogeneous Strain in the Multiferroic $BiFeO_3$, Phys. Rev. Lett. **112**, 097602 (2014).

[25] S. H. Lee, A. L. Cavalieri, D. M. Fritz, M. C. Swan, R. S. Hegde, M. Reason, R. S. Goldman, and D. A. Reis, Generation and Propagation of a Picosecond Acoustic Pulse at a Buried Interface: Time-Resolved X-Ray Diffraction Measurements, Phys. Rev. Lett. **95**, 246104 (2005).

[26] H. Wen, P. Chen, M. P. Cosgriff, D. A. Walko, J. H. Lee, C. Adamo, R. D. Schaller, J. F. Ihlefeld, E. M. Dufresne, D. G. Schlom, P. G. Evans, J. W. Freeland, and Y. Li, Electronic Origin of Ultrafast Photoinduced Strain in $BiFeO_3$, Phys. Rev. Lett. **110**, 037601 (2013).

[27] D. Daranciang, M. J. Highland, H. Wen, S. M. Young, N. C. Brandt, H. Y. Hwang, M. Vattilana, M. Nicoul, F. Quirin, J. Goodfellow, T. Qi, I. Grinberg, D. M. Fritz, M. Cammarata, D. Zhu, H. T. Lemke, D. A. Walko, E. M. Dufresne, Y Li, J. Larsson, D. A. Reis, K. Sokolowski-Tinten, K. A. Nelson, A. M. Rappe, P. H. Fuoss, G. B. Stephenson, and A. M. Lindenberg, Ultrafast Photovoltaic Response in Ferroelectric Nanolayers, Phys. Rev. Lett. **108**, 087601 (2012).

[28] S. Matzen, L. Guillemot, T. Maroutian, S. K. K. Patel, H. Wen, A. D. DiChiara, G. Agnus, O. G. Shpyrko, E. E. Fullerton, D. Ravelosona, P. Lecoeur, and R. Kukreja, Tuning ultrafast photoinduced strain in ferroelectric-based devices, Adv. Electron. Mater. **5**, 1800709 (2019).

[29] H. Akamatsu, Y. Yuan, V. A. Stoica, G. Stone, T. Yang, Z. Hong, S. Lei, Y. Zhu, R. C. Haislmaier, J. W. Freeland, L-Q Chen, H. Wen, and V. Gopalan, Light-Activated Gigahertz Ferroelectric Domain Dynamics, Phys. Rev. Lett. **120**, 096101 (2018)

[30] A. Arbouet, G. M. Caruso, and F. Houdellier, Ultrafast Transmission Electron Microscopy: Historical Development, Instrumentation, and Applications, in *Advances in Imaging and Electron Physics*, edited by P. W. Hawkes, Vol. 207 (Elsevier, 2018), Chap. 1, pp. 1–342.

[31] A. Feist, N. R. da Silva, W. Liang, C. Ropers, and S. Schäfer, Nanoscale diffractive probing of strain dynamics in ultrafast transmission electron microscopy, Struct. Dyn. **5**, 014302 (2018).

[32] A. Nakamura, T. Shimojima, M. Matsuura, Y. Chiashi, M. Kamitani, H. Sakai, S. Ishiwata, H. Li, A. Oshiyama, and K. Ishizaka, Evaluation of photo-induced shear strain in monoclinic VTe2 by ultrafast electron diffraction, Appl. Phys. Express **11**, 092601 (2018).

[33] H. T. Lemke, D. W. Breiby, T. Ejdrup, P. Hammershøj, M. Cammarata, D. Khakhulin, N. Rusteika, S-I. Adachi, S. Koshihara, T. S. Kuhlman, S. O. Mariager, T. N. Nielsen, M. Wulff, T. I. Sølling, N. Harrit, R. Feidenhans, and M. M. Nielsen, Tuning and tracking of coherent shear waves in molecular films, ACS Omega **3**, 9929-9933 (2018).

[34] See Supplemental Material at http://link.aps.org/supplemental/10.1103/PhysRevB.102.220303 for the description of the seven notes. Note 1: crystallographic frames, note 2: longitudinal and shear strain in the unit cell, note 3: Bragg peak shift in grazing incidence, note 4: photoinduced acoustic waves propagation in an anisotropic medium, note 5: x-ray beam path in the grazing incidence geometry, note 6: acoustic waves photogeneration processes, and note 7: light-induced temperature increase in the BFO crystal.

[35] M. Lejman, G. Vaudel, I. C. Infante, I. Chaban, T. Pezeril, M. Edely, G. F. Nataf, M. Guennou, J. Kreisel, V. E. Gusev, B. Dkhil, and P. Ruello, Ultrafast acousto-optic mode conversion in optically birefringent ferroelectrics, Nat. Commun. **7**, 12345 (2016).

[36] B. Kundys, M. Viret, D. Colson, and D. O. Kundys, Light-induced size changes in $BiFeO_3$ crystals, Nature Mater. **9**, 803 (2010).

[37] S. G. Choi, H. T. Yi, S.-W. Cheong, J. N. Hilfiker, R. France, and A. G. Norman, Optical anisotropy and charge-transfer transition energies in $BiFeO_3$ from 1.0 to 5.5 eV, Phys. Rev. B **83**, 100101(R) (2011).

[38] C. Laulhé, M. Cammarata, M. Servol, R. J. Dwayne Miller, M. Hada, and S. Ravy, Impact of laser on bismuth thin-films, Eur. Phys. J.: Spec. Top. **222**, 1277 (2013).

[39] The absorption length of the x-ray beam has been calculated on the basis of tabulated data found at http://www.cxro.lbl.gov//

[40] K. Medjoubi, S. Hustache, F. Picca, J. F. Bérar, N. Boudet, F. Bompard, P. Breugnon, J.-C. Clémens, A. Dawiec, and P. Delpierre, Performance and applications of the CdTe- and Si-XPAD3 photon counting 2D detector, J. Inst. **6**, C01080 (2011).

[41] C. Thomsen, H. T. Grahn, H. J. Maris, and J. Tauc, Surface generation and detection of phonons by picosecond light pulses, Phys. Rev. B **34**, 4129 (1986).

[42] E. Borissenko, M. Goffinet, A. Bosak, P. Rovillain, M. Cazayous, D. Colson, P. Ghosez, and M. Krisch, Lattice dynamics of multiferroic BiFeO3 studied by inelastic x-ray scattering, J. Phys.: Condens. Matter **25**, 102201 (2013).

[43] S. L. Shang, G. Sheng, Y. Wang, L. Q. Chen, and Z. K. Liu, Elastic properties of cubic and rhombohedral BiFeO3 from first-principles calculations, Phys. Rev. B **80**, 052102 (2009).

[44] A. Palewicz, I. Sosnowska, R. Przenioslo, and A. W. Hewat, $BiFeO_3$ Crystal Structure at low temperatures, Acta Phys. Pol., A **117**, 296 (2010).

[45] S. Gómez-Salces, F. Aguado, F. Rodríguez, R. Valiente, J. González, R. Haumont, and J. Kreisel, Effect of pressure on the band gap and the local FeO_6 environment in $BiFeO_3$, Phys. Rev. B **85**, 144109 (2012).

[46] C. Paillard, B. Xu, B. Dkhil, G. Geneste, and L. Bellaiche, Photostriction in Ferroelectrics from Density Functional Theory, Phys. Rev. Lett. **116**, 247401 (2016).

[47] S. Murakami, T. Yoshimura, K. Satoh, K. Wakazono, K. Kariya, and N. Fujimura, Development of piezoelectric MEMS vibration energy harvester using (100) oriented $BiFeO_3$ ferroelectric film, J. Phys.: Conf. Ser. **476**, 012007 (2013).

[48] R. J. Sichel, Structural and electromechanical properties of epitaxial $BiFeO_3$ thin films, Ph.D. dissertation, University of Wisconsin, 2011.

[49] Z. Chen, S. Prosandeev, Z. L. Luo, W. Ren, Y. Qi, C. W. Huang, L. You, C. Gao, I. A. Kornev, T. Wu, J. Wang, P. Yang, T. Sritharan, L. Bellaiche, and L. Chen. Coexistence of ferroelectric triclinic phases in highly strained BiFeO3 films, Phys. Rev. B **84**, 094116 (2011).